Received: 10 September 2021 | Revised: 5 April 2022 | Accepted: 6 June 2022 | Published on: 10 July 2022

DOI: 10.1002/qj.4333

Quarterly Journal of the Royal Meteorological Society RMetS

RESEARCH ARTICLE

Assessing the importance of mesoscale sea-surface temperature variations for surface turbulent cooling of the Kuroshio Extension in wintertime

Sydney Sroka[1] | **Arnaud Czaja**[2] | **Soumi Chakravorty**[2]

[1]Department of Mechanical Engineering, Massachusetts Institute of Technology, Cambridge, MA, USA

[2]Department of Physics, Imperial College, London, UK

Correspondence
Sydney Sroka, Department of Mechanical Engineering, Massachusetts Institute of Technology, Cambridge, MA, 02139, USA.
Email: ssroka@mit.edu

Abstract

Western boundary currents are well known to exhibit a strong eddy field and meandering on subseasonal timescales and wavelengths of a few hundreds of kilometers. However, the extent to which the ocean mesoscale activity associated with these motions can enhance the turbulent air–sea heat flux averaged over a large spatial domain has not been fully characterized. This study aims to do so during the cold season using reanalysis data and simplified air–sea interaction models. The correlation between sea-surface height anomaly and the wintertime mean heat fluxes does not indicate any significant relations between eddy activity and large-scale surface heat flux in the Kuroshio Extension during winter over the 2003–2018 period. The results from simple models designed to isolate the contributions from the eddies suggest that the eddy enhancement of the heat flux via a rectified effect (a bit more anomalous cooling over a warm mesoscale feature than anomalous heating over a cold one) is small compared with the long-time, large-spatial scale mean in the reanalysis data, especially along the Kuroshio Extension. It is found larger north of it, where it can reach $5\,\mathrm{W{\cdot}m^{-2}}$. Although different datasets might disagree about the level of energy of the sea-surface temperature field at the mesoscale, a simple scaling analysis gives confidence in the relatively small values of the rectified effect found here.

KEYWORDS

air-sea interaction, ERA5, ocean mesoscale eddies, rectified effect

1 | INTRODUCTION

The western boundary currents of the World Ocean provide an important heat source for the atmospheric storm-track (Hoskins and Valdes, 1990). Regions with strong currents, like the Kuroshio Extension (KE) or Gulf Stream, can be expected to modify the wind stress by as much as 20%, which has significant implications for the air–sea heat flux in those regions (Chelton *et al.*, 2004). This study focuses on the North Pacific, and specifically the Kuroshio, in winter, when the atmospheric eddy-driven jet is closest to the path of the Kuroshio and its

extension into the interior of the Pacific (Nakamura *et al.*, 2004).

Though large-scale (>1,000 km) correlations between sea-surface temperature (SST) and surface winds are generally negative, observations and simulations have confirmed a strong positive correlation at the mesoscale (Chelton and Xie, 2010). Chelton *et al.* (2004), and subsequent studies including O'Neill *et al.* (2010), identified persistent, small-scale structures from high-resolution (25 km) satellite measurements of surface winds and found that there were many features with characteristic wavelengths less than 30° in longitude and 10° in latitude that could be attributed to SST variations. The authors showed how the curl and divergence of the 4-year averaged wind field were directly proportional to the downwind and crosswind gradient of the SST field, respectively.

Putrasahan *et al.* (2013) isolated the influence of ocean mesoscale eddies on surface winds in the KE region by conducting companion simulations with a regional model where eddies are either resolved or filtered out. Their results showed that the eddies play an important role in driving the surface wind through two mechanisms: vertical mixing from alternating regions of boundary layer stability and sea-level pressure anomalies. The strength of the former mechanism, which is measured by the magnitude of the linear scaling between the wind stress divergence (curl) and downwind (crosswind) SST gradient, was found to exhibit a strong seasonality, being much larger in the winter, when the atmosphere is generally less stable, than in the summer. The simulations exhibited a steeper linear relationship than was calculated from satellite observations, but the findings strongly supported the conclusion that the mesoscale eddies are an important driver of surface wind stress. With regard to the latter pressure-driven mechanism, which is measured by the linear scaling of the wind convergence and the sea-level pressure Laplacian, the authors found that the presence of eddies significantly strengthened the ocean–atmosphere coupling compared with the eddy-free simulation.

It has recently been suggested that the meanders or eddies that develop on western boundary currents with characteristic length scales of a few hundred kilometers have a so-called rectified effect on the turbulent air–sea heat flux Q because a little bit more heat is lost over a warm anticyclone than is gained over a cold cyclone (Small *et al.*, 2008; Foussard *et al.*, 2019). This then was suggested to have a significant effect on the storm track, at least in the North Pacific (X. Ma *et al.*, 2015; 2017; Zhang *et al.*, 2020) and South Atlantic (Villas Bôas *et al.*, 2015). Small *et al.* (2008) reviewed various physical mechanisms that facilitate air–sea heat flux from ocean eddies and fronts, including the destabilizing effect of air traveling over SST gradients, large eddies increasing the boundary-layer depth, secondary circulations associated with spatial changes in the pressure-gradient force, and the way changes in ocean surface velocities can locally increase the surface stress. The source of SST anomalies near strong SST frontal regions like the Kuroshio–Oyashio Extension region is thought to be oceanic weather rather than atmospheric forcing (Frankignoul, 1985; Bishop *et al.*, 2017).

Isolating the effect of ocean mesoscale eddies on the turbulent heat fluxes from observations is difficult because, unlike in an atmospheric general circulation model, one cannot separately analyze a time history of the heat flux with and without eddies, as was done in Putrasahan *et al.* (2013) or Foussard *et al.* (2019), for example. In this article, we propose a new methodology that attempts to do so by developing simplified models of air–sea interactions tuned to realistic air–sea heat fluxes. The models use just one or two eddy coupling coefficients, so it is straightforward to evaluate the effect of the eddies on the time mean and spatially averaged Q. The first model represents the eddy enhancement as an increase in the surface wind speed and is based on the work from O'Neill *et al.* (2010), who used wind vector and SST observations to estimate the wind vector magnitude and direction response to the persistent mesoscale eddies near western boundary currents. The authors found that air flow along a positive (negative) SST gradient led to an acceleration (deceleration) and anticyclonic (cyclonic) changes in the wind velocity; the magnitudes of changes in the wind velocity and direction were about 1–2 $m \cdot s^{-1}$ and 4°–8°. The second model adds a mechanism to the first model such that the eddy enhancement can also be represented through an increase in the sea-surface drag following Behringer *et al.* (1979). Small *et al.* (2008) discuss several studies that consider the mechanism by which warmer SSTs lead to atmospheric instabilities that increase the local sea-surface drag coefficient and, therefore, the stress. The emerging consensus appears to be that an increase in the sea-surface drag with SST is a much smaller contribution to the increase in surface stress compared with other mechanisms, like a pressure-gradient-driven increase in the surface wind speed.

This article is structured as follows. We introduce the data used for the air–sea interaction analysis in Section 2 and discuss the impact of the mesoscale ocean eddy activity on the time and spatial mean Q in Section 3. Section 4 introduces the interaction models and shows that the models are able to well represent the time mean air–sea turbulent heat flux over the KE in winter. Discussion and conclusion sections are offered in Sections 5 and 6, respectively.

2 | DATA AND METHODS

The ERA5 reanalysis data (Hersbach *et al.*, 2018; 2020; downloaded from the Copernicus Climate Change Service Climate Data Store) was extracted at a 0.25° spatial resolution and at a 6-hr temporal resolution for the boreal winter months December through March (DJFM) over the period 2003–2018. The region considered is a patch of the Northwest Pacific Ocean (30° N to 41.5° N, 142.5° E to 169° E) that captures the major features of the KE. The reanalysis fields include the SST T_o, the temperature at 2 m T_a, the surface pressure p_0, the dew-point temperature at 2 m T_d, the surface wind vector $[u, v]$, the surface sensible heat flux Q_s, and the surface latent heat flux Q_L. In addition, daily absolute topography (hereafter simply denoted as "sea-surface height anomaly", SSHA) from the E.U. Copernicus Marine Service Information (Drévillon *et al.*, 2018; Global Monitoring and Forecasting Center, 2018) was used for the analysis in Section 3.

A two-dimensional fast Fourier transform (FFT) filter was used to separate the high from the low wave numbers in the field variables from the reanalysis data for each of the models. The filtering scheme used here is similar to the one used in Scott and Wang (2005). First, a bilinear plane is calculated with a least-squares fit to $c_0 + c_1x + c_2y$, where c_i variables are constants and x and y are the zonal and meridional directions, respectively. This plane is subtracted from the field to spatially de-mean and de-trend the data. Next, a two-dimensional FFT is applied. The cutoff wave number is the radius of a circle centered on the origin of the transformed field, and the low-pass (high-pass) field is recovered by removing all the wave numbers outside (inside) of this circle and then inverting the transform. A filter length scale of 500 km, or wave number equal to 0.002 km^{-1}, was used for all field variables to separate the eddy length scales from the large scales. The filter is applied to each time step before any time averaging is done. The bilinear plane is added to the low-pass field after the inverse transform step. High-pass fields are denoted with primes ($\bullet'$), and low-pass fields are denoted with overbars ($\overline{\bullet}$).

This filtering procedure leads to several important properties of the filtered output. It ensures that the original signal is equal to the sum of its low-pass and high-pass components ($\bullet = \overline{\bullet} + \bullet'$), that low-pass filtering a single high-pass filtered field vanishes ($\overline{\bullet'} = 0$), and that low-pass filtering a field that was already low-pass filtered does not change the output ($\overline{(\overline{\bullet})} = \overline{\bullet}$). However, it is important to note that low-pass filtering the product of a low-pass filtered field and a high-pass filtered field does not guarantee the result vanishes ($\overline{\overline{\bullet}\bullet'} \neq 0$); this can be illustrated with a simple, one-dimensional example. If a signal $s(x)$, where x measures horizontal distance, is the sum of two cosine functions with wave numbers k_1 and k_2, and the cutoff wave number k_c is such that $k_1 > k_c > k_2$, then

$$s(x) = \cos(k_1 x) + \cos(k_2 x). \tag{1}$$

After applying the spectral filter described earlier, we obtain

$$\bar{s}(x) = \cos(k_2 x) \quad \text{and} \quad s'(x) = \cos(k_1 x), \tag{2}$$

and as a result

$$\begin{aligned} \bar{s}(x)s'(x) &= \cos(k_2 x)\cos(k_1 x) \\ &= \frac{\cos[(k_1 + k_2)x] + \cos[(k_1 - k_2)x]}{2}. \end{aligned} \tag{3}$$

Since $k_1 + k_2$ is guaranteed to be greater than k_c, whether $\overline{\bar{s}s'}$ vanishes depends on whether $|k_1 - k_2|$ is greater than or less than k_c. In an atmospheric context, extinguishing $\overline{\bar{s}s'}$ is guaranteed by considering the zonal mean (i.e., $k_c = 0$). For the regional reanalysis datasets considered here, however, no products of high-passed and low-passed fields are expected to vanish after low-pass filtering due to the broad range of wave-number content around the eddy scale (Scott and Wang, 2005; Tulloch *et al.*, 2011).

The procedure is illustrated for the SST field on a random winter day in Figure 1. The raw data is shown in Figure 1a and its decomposition into high-pass and

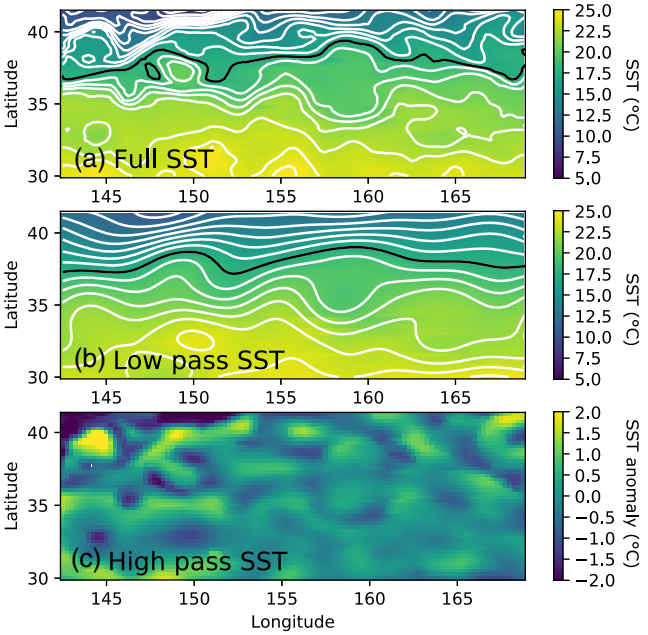

FIGURE 1 The sea-surface temperature (SST, ° C) field and its spectral decomposition on December 2, 2010, at 0600 UTC. (a) Raw data; (b) low-pass and (c) high-pass components. The contour interval in (a) and (b) is 1° C [Colour figure can be viewed at wileyonlinelibrary.com]

low-pass components (including the bilinear plane) are shown in Figure 1b and Figure 1c, respectively. The sharp front associated with the Oyashio current is clearly seen in the northwest corner of the domain around 40° N, as is the weaker imprint of the Kuroshio on the SST gradient just north of it along 36° N in Figure 1a. The low-pass field in Figure 1b somewhat merges these two fronts, but it captures the long wavelength meanders along the Kuroshio observed between 152° E and 160° E. The high-pass field in Figure 1c displays more energy north of 35° N, with some features clearly associated with a sharpening the Oyashio and Kuroshio SST fronts (the two dipoles seen north of 38° N and the zonally elongated dipole along approximately 36° N), and some other features tentatively interpreted as being detached mesoscale eddies (e.g., the "cold eddy" seen at 144° E, 33° N with an amplitude of 1.5° C).

3 | CORRELATIONS BETWEEN THE SSHA CONTOUR LENGTH AND THE TURBULENT HEAT FLUX

This analysis uses the length of the SSHA contours as a proxy for the amount of eddy activity along the KE. As shown by Qui and co-workers (Qiu and Chen, 2005; Qiu *et al.*, 2020), the SSHA contours indicate the Kuroshio's path. Qiu *et al.* (2020) labels the Kuroshio's path for all years from 1992 through 2019 as either stable, when there was very little change in the contours' locations, or unstable, when there were large fluctuations in the SSHA contours throughout the year. In unstable years, the contours' large fluctuations result in a longer average length and much more curvature than those from stable years, as seen in Qiu *et al.* (2020, fig. 2). Years where the trajectories of the contours are more dynamic are also associated with increased eddy activity, as the scale and locations of the mesoscale SST anomalies are reflected in the curvature of the SSHA contours.

The results of a correlation analysis do not suggest that increased eddy activity leads to a greater wintertime mean heat flux in the reanalysis data through the rectified effect discussed in Section 1. A representative contour plot of SSHA is shown in Figure 2a. The 0.4 m contour, highlighted in white in Figure 2a, was chosen for its proximity to the largest SST gradient, which indicates the main path of the Kuroshio. Figure 2b shows a scatterplot of the winter time mean turbulent heat flux (raw data, no spatial filtering applied) as a function of the length of the 0.4 m contour. The length of the contour level was calculated at daily intervals and then averaged over each DJFM winter. The time mean heat flux for each winter in the region is computed from the reanalysis sensible and latent surface heat flux fields. As expected, the lengths of the 0.4 m contour in unstable years (blue crosses) are nearly all longer than those of stable years (red crosses), these years having been selected based on Qiu *et al.* (2020). The Pearson correlation coefficients between the contour length and the wintertime mean heat fluxes for the stable years, unstable years, and all years are −0.33, −0.11, and −0.18, respectively. The correlation coefficients are all slightly negative, which is reflected in the linear fits shown in Figure 2b, but none are found to be statistically significant. Though not statistically significant, a negative correlation would suggest that an increase in eddy activity decreases the heat flux rather than enhances it, as the rectified effect hypothesis would predict (Ma *et al.*, 2016; 2017).

We have repeated this analysis with different choices of SSHA contours (0.3 m and 0.5 m) as well as with the northern and southern halves of the domain, their difference, and also with a box centered on the middle of the domain, rather than the full domain (Table 1). In no cases were we able to find a statistically significant relation between

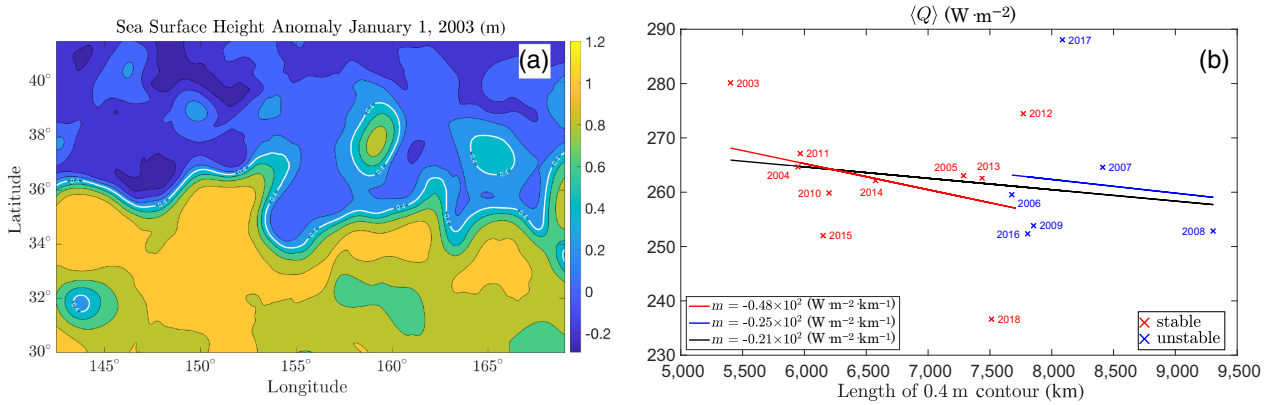

FIGURE 2 (a) Sea-surface height anomaly on January 1st 2003 (m). (b) Scatterplot of the average wintertime mean turbulent heat flux (in W/m^2) of the region shown in (a) as a function of the length of the 0.4 m contour in the same region. The slopes m of the linear fits for the stable (red), unstable (blue), and all (black) years are indicated in the legend [Colour figure can be viewed at wileyonlinelibrary.com]

TABLE 1 Results of linear regression analyses between the length of the sea-surface height anomaly (SSHA) contours (columns, in meters) and spatially averaged surface turbulent heat flux (positive upward). The values of the slopes are given in units of $W{\cdot}m^{-2}{\cdot}km^{-1}$ with the associated *P*-value in parentheses. The domains are defined as follows: N is (142.5°–169° E, 37.67°–41.5° N), M is (142.5°–169° E, 33.8°–37.67° N), and S is (142.5°–169° E, 30°–33.8° N)

Domain versus SSHA contour	0.3 m	0.4 m	0.5 m
N + S	−40 (0.16)	−21 (0.49)	−3 (0.93)
N	−19 (0.47)	−7 (0.8)	19 (0.59)
M	−56 (0.15)	−26 (0.54)	2 (0.97)
S	−44 (0.27)	−30 (0.48)	−31 (0.56)
N − S	45 (0.4)	23 (0.66)	50 (0.43)

the length of the SSHA contour and the spatially averaged turbulent heat flux (large *P*-values; see the numbers in parentheses in Table 1).

These results suggest that there is little relation between the dynamical state of the KE and surface turbulent cooling in the Northwest Pacific. Even the intuitive association between more meandering and possibly warm (cold) eddies crossing northward (southward) across the Kuroshio front, leading to more cooling north of the KE front and less cooling south of it (Ma *et al.*, 2016), is not supported by our analysis (the slope of the regression is positive for the "N–S box" in Table 1 but the *P*-value is large). A similar decoupling between the state of the KE system and regional surface turbulent cooling was suggested by Qiu and Chen (2006) in their analysis of the decadal variability of subtropical mode water formation.

This negative result does not, however, rule out the possibility that the mesoscale structures, either in the form of isolated eddies or quasi-stationary fronts *north* of the KE, have an impact on the surface turbulent heat flux over this region through the rectified effect discussed in Section 1. Indeed, as found in other western boundary currents, the largest SST gradients are found north of the KE and the stirring of the SST contours by geostrophic turbulence there might be unrelated to the dynamical state of the KE to the south. In addition, as is well known from previous studies of turbulent heat flux variability (e.g., Cayan, 1992), there is a significant control on the variability of the surface cooling by atmospheric dynamics through changes in wind speed, air temperature, and moisture. These would also obscure any links between the state of the KE and the surface turbulent heat flux in the Northwest Pacific.

To help in isolating the oceanic mesoscale contribution to surface turbulent cooling in the Northwest Pacific, we next construct simplified models of the latter, which we test against reanalysis data.

4 | MODEL RESULTS

4.1 | The β-model

The first model, the β-model, solely accounts for the observations by Chelton *et al.* (2004) and O'Neill *et al.* (2010) that perturbations of surface wind speed and SST are positively correlated on the oceanic mesoscale. If β is the coupling coefficient measuring the strength of this relation, we write $U' = \beta T'_o$ where U' is the perturbation wind speed, T'_o is the high-pass-filtered SST from the reanalysis data, and $\beta > 0$ is a constant. Accordingly, our first model is

$$Q^{\beta} = \rho_a C_E(\overline{U} + \beta T'_o)\Delta h, \tag{4}$$

where Q^{β} is the sum of the surface sensible heat flux and surface latent heat flux, C_E is a constant exchange coefficient, ρ_a is the density of air, and $\overline{U}$ is the low-pass-filtered magnitude of the horizontal surface wind vector $\|(u, v)\|$. The moist enthalpy potential Δh is $c_p(T_o - T_a) + L_v(q^*_o - q_a)$, where c_p is the specific heat of air, T_o is the SST, L_v is the latent heat of vaporization, q^*_o is the saturation specific humidity at T_o, and q_a is the specific humidity at T_a and T_d.

An interior-point optimization scheme is used to solve for the exchange coefficient C_E and the eddy coupling coefficient β. The optimization is performed separately for each DJFM winter, yielding wintertime time series for the parameters C_E and β. Specifically, we minimize the magnitude of the objective function J:

$$J([\beta, C_E]) = Q^{\mathrm{ERA5}}(x, y, t) - Q^{\beta}(x, y, t; [\beta, C_E]), \tag{5}$$

where $Q^{\mathrm{ERA5}}(x, y, t)$ is the sum of the surface sensible and latent heat flux fields from the reanalysis data. An analogous objective function is used for the subsequent model. The mean and standard deviation of β across all winters is found to be $0.25 \pm 0.03\ m{\cdot}s^{-1}{\cdot}K^{-1}$. The values of the exchange coefficient C_E are very consistent between winters, with a mean and standard deviation of $1.4 \pm 0.01 \times 10^{-3}$.

The simple β-model is successful at representing the wintertime mean (denoted with angle brackets $\langle\bullet\rangle$) turbulent heat flux, as shown in Figure 3, especially in the center of the selected domain where the heat flux is largest. The results are only shown here for two distinct winters (2003 in the top row and 2007 in the bottom row) but are consistent across all years. These two years are excellent examples of when the path of the Kuroshio did not change much (2003) and when the path exhibited

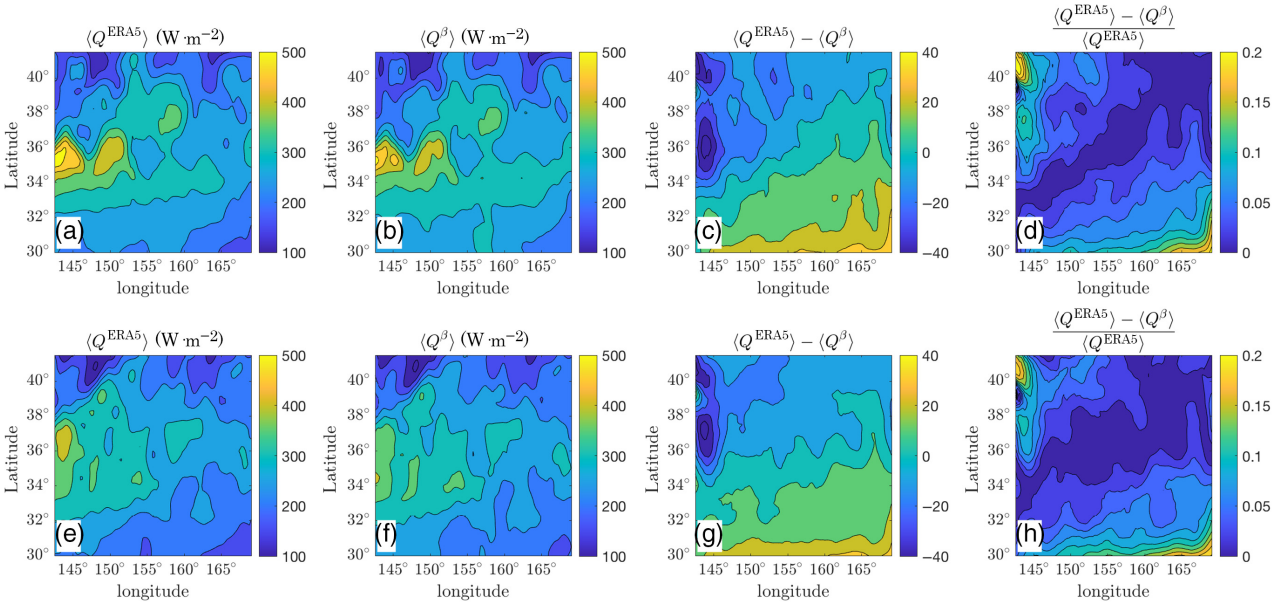

FIGURE 3 (a, e) The time mean turbulent heat flux from ERA5, (b, f) the time-averaged turbulent heat flux from the β-model, (c, g) their difference, and (d, h) pointwise relative error for the winters of (a–d) 2003 and (e–h) 2007. Heat fluxes are expressed in $W \cdot m^{-2}$ [Colour figure can be viewed at wileyonlinelibrary.com]

many large fluctuations (2007) throughout the year. Consistent with Figure 2, the larger surface turbulent cooling of the ocean in 2003 is associated with a meridionally narrower structure and less meandering of the Kuroshio than in 2007. Note that the absolute errors (center right panels) are less than $20\,W \cdot m^{-2}$ (relative errors less than 10% seen in the right panels) over most of the domain, except in the northwestern and southeastern corners where they reach about 20%.

The time dependence of the model within a given winter is further illustrated in Figure 4, which displays the time series of Q_β (continuous green) and the actual Q from ERA5 (blue) at 148.5° E, 41° N. The agreement between the two curves is excellent and, anticipating slightly on the results below, arise because the bulk of the surface cooling is controlled by the large scale fields which are used as input into the model. Accordingly, very similar results are found if different locations are used (not shown).

To study the sensitivity of the model's results to changes in the β parameter, the root-mean-squared error (RMSE) is calculated between the time mean heat flux from ERA5 and the time mean heat flux from the model using a scaled value for β. For each year the RMSE is

$$\mathrm{RMSE} = \sqrt{\frac{1}{N}\sum_{i=1}^{N}(\langle Q^{\mathrm{ERA5}}\rangle^i - \langle Q^{\beta}(\gamma\beta)\rangle^i)^2}, \qquad (6)$$

where N is the total number of spatial points in the region of interest (the model is evaluated on the ERA5 grid, which recall has a resolution of 0.25°) and the scaling parameter γ varies from −10 to +10. The RMSEs between the reanalysis and the model as a function of the scaled β are shown in Figure 5a, and each curve corresponds to a separate winter. The RMSE of the unscaled model ($\gamma = 1$) is shown with a filled black circle for each year. For these sensitivity tests, C_E is held at its optimized value for each winter, although, as previously mentioned, the variance in C_E among winters is quite small.

These results show a clear optimality near a value of $\beta = +0.25\,m \cdot s^{-1} \cdot {}^\circ\,C^{-1}$ which falls in between the observational estimate by O'Neill *et al.* (2010) of $+0.3\,m \cdot s^{-1} \cdot {}^\circ\,C^{-1}$ (see their fig. 3a) and the model results by Zhang *et al.* (2020) of $+0.21\,m \cdot s^{-1} \cdot {}^\circ\,C^{-1}$. J. Ma *et al.* (2015) quote even higher values in their observational study of up to $\beta = +0.39\,m \cdot s^{-1} \cdot {}^\circ\,C^{-1}$, but we are nevertheless encouraged that our optimization provides a consistent and physically plausible value.

To provide further support for the model, we have repeated the calculation with a coarser reanalysis dataset, namely the National Centers for Environmental Prediction (NCEP)–National Center for Atmospheric Research (NCAR) reanalysis project (Kalnay *et al.*, 1996). This dataset is provided on a Gaussian grid with approximately 1.8° (1.9°) resolution in longitude (latitude); that is, almost an order of magnitude coarser than ERA5. The results, displayed in Figure 5b, show that a similar skill is found, with RMSEs on the order of $10–20\,W \cdot m^{-2}$. Interestingly, however, the parabolas are much flatter, which indicate that there is less "leverage" from T_0' to reduce errors in this dataset compared with ERA5. The optimized value of β is

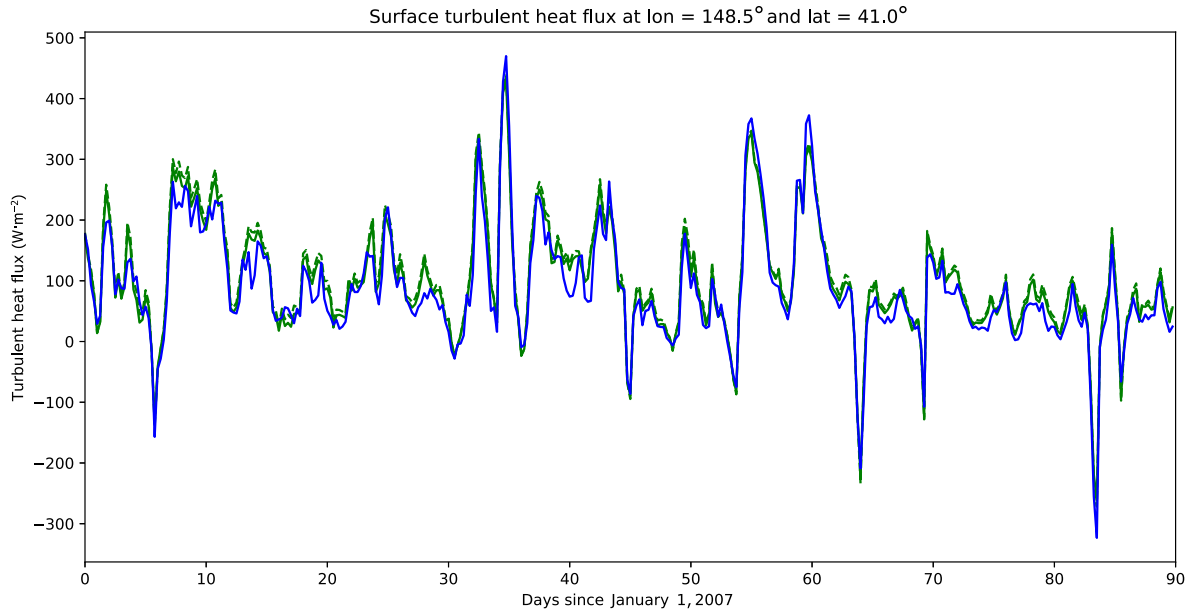

FIGURE 4 Time series of six-hourly surface turbulent heat flux at 148.5° E, 41° N for (continuous blue) ERA5 and (continuous green) Q_β. The dashed green curve displays the modeled time series when β is set to zero [Colour figure can be viewed at wileyonlinelibrary.com]

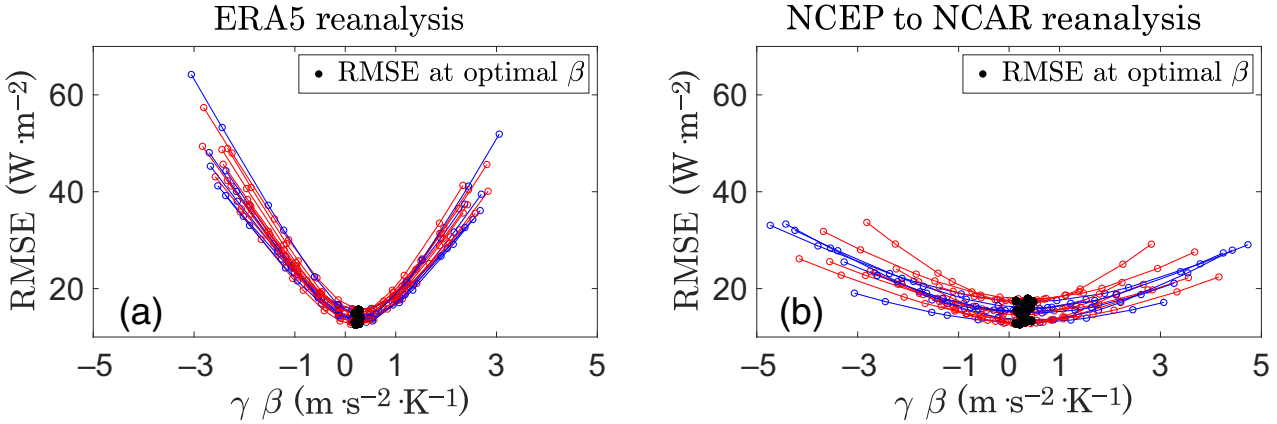

FIGURE 5 The root-mean-squared-error (RMSE) between the time mean turbulent heat flux from reanalysis data and the β-model with scaled values of β. The RMSEs from years when the Kuroshio was stable are connected with red lines, and those from unstable years are connected with blue lines. The RMSE using the optimal value of β (i.e., $\gamma = 1$) is shown with a filled black circle for each year. (a) ERA5 and (b) National Centers for Environmental Prediction (NCEP)–National Center for Atmospheric Research (NCAR) calculation [Colour figure can be viewed at wileyonlinelibrary.com]

also less consistent between winters in NCEP–NCAR than in ERA5. Both results are consistent with our expectations that at the coarser spatial resolution there is little energy in T_o' such that we would not expect as great an impact of the mesoscale signals in modulating the surface turbulent heat flux. This result and the consistency and physically plausible values of β found using ERA5 give us confidence in the model and motivate us to further use it to isolate the mesoscale contribution to wintertime surface cooling over the Kuroshio.

The years where the Kuroshio is considered stable and unstable are again shown in red and blue, respectively, in Figure 5. There is no clear relationship between the RMSE and the stability, reinforcing the conclusion from Section 3 that there is little connection between the wintertime turbulent air–sea heat flux and the level of mesoscale eddy activity over the Kuroshio in the ERA5 dataset. To isolate the contribution of mesoscale features to surface cooling more quantitatively, we decompose the spatially averaged (low-pass-filtered) surface turbulent heat flux as (following the notation in Section 2)

$$\overline{Q^\beta} = \overline{\rho_a C_E (\overline{U} + \beta T_o')(\overline{\Delta h} + \Delta h')}$$

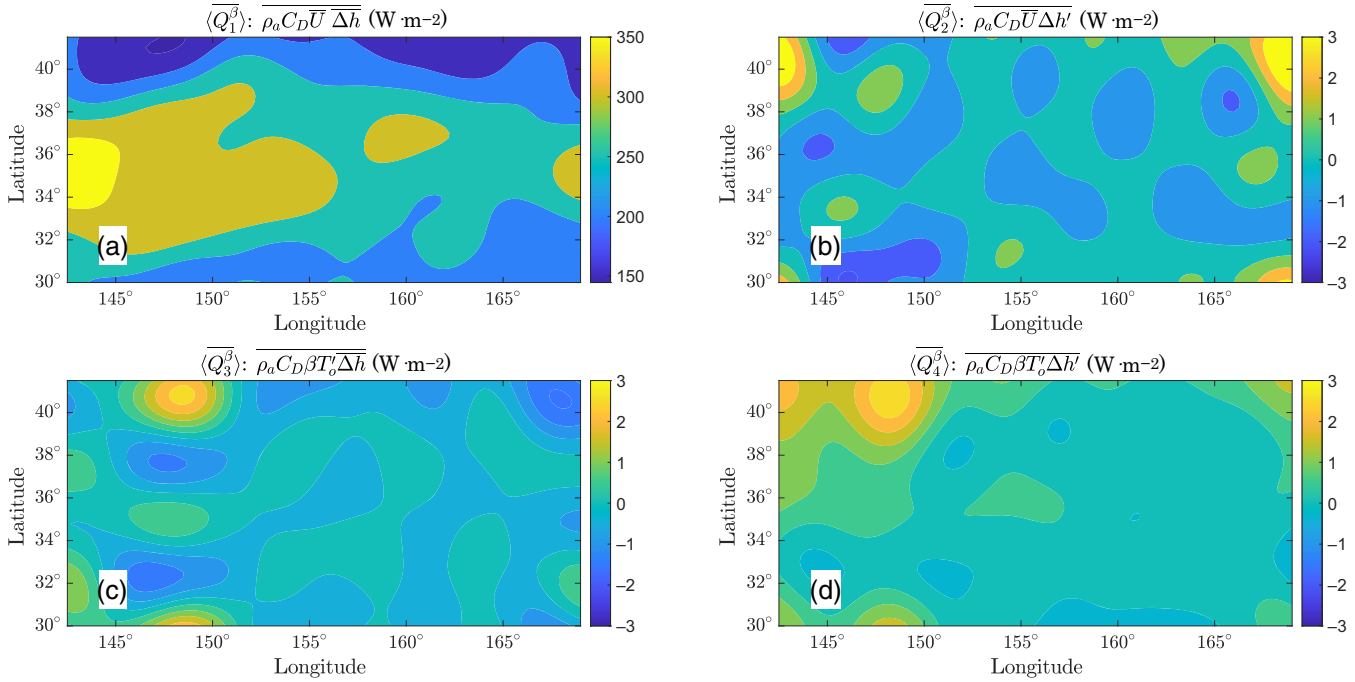

FIGURE 6 The wintertime mean of the β-model terms for 2007: (a) the long-time, large spatial-scale term $\langle\overline{Q_1^\beta}\rangle$, (b) the persistent temperature anomaly term $\langle\overline{Q_2^\beta}\rangle$, and the two rectified effect terms (c) $\langle\overline{Q_3^\beta}\rangle$ and (d) $\langle\overline{Q_4^\beta}\rangle$. Note the different scales of the color bar in (a) compared with (b)–(d) [Colour figure can be viewed at wileyonlinelibrary.com]

$$
\begin{aligned}
&= \overline{\rho_a C_E(\overline{U}\ \overline{\Delta h} + \overline{U}\Delta h' + \beta T_o' \overline{\Delta h} + \beta T_o' \Delta h')} \\
&= \underbrace{\overline{\rho_a C_E \overline{U}\ \overline{\Delta h}}}_{\overline{Q_1^\beta}} + \underbrace{\overline{\rho_a C_E \overline{U} \Delta h'}}_{\overline{Q_2^\beta}} \\
&\quad + \underbrace{\overline{\rho_a C_E \beta T_o' \overline{\Delta h}}}_{\overline{Q_3^\beta}} + \underbrace{\overline{\rho_a C_E \beta T_o' \Delta h'}}_{\overline{Q_4^\beta}}. \qquad (7)
\end{aligned}
$$

Contour plots of the wintertime mean for each of the terms in Equation 7 from 2007, which was a particularly unstable year, are shown in Figure 6. These results show that the long-time, large spatial-scale term $\langle\overline{Q_1^\beta}\rangle$ is the dominant contributor. The eddy-enhancement terms $\langle\overline{Q_3^\beta}\rangle$ and $\langle\overline{Q_4^\beta}\rangle$ (both proportional to β) are largest on the west side of the domain where the eddy activity is most pronounced, but the magnitude of the flux from these terms is much smaller than that from $\langle\overline{Q_1^\beta}\rangle$. Recall that $\langle\overline{Q_2^\beta}\rangle$ and $\langle\overline{Q_3^\beta}\rangle$ do not vanish because the spatial frequency content of the product of a low-pass field and a high-pass field includes frequencies below the cutoff. The term $\langle\overline{Q_4^\beta}\rangle$ is the most intuitively connected to the rectified effect as it is proportional to $T_o'\Delta h'$. Figure 6 indicates, nevertheless, that the other term proportional to β, namely $\langle\overline{Q_3^\beta}\rangle$, is adding to $\langle\overline{Q_4^\beta}\rangle$ with a similar magnitude. As emphasized in Section 2, this term arises out of the filtering procedure. Together, their sum represents the total rectified effect of mesoscale eddies on the turbulent heat flux. The sum is shown in Figure 7a and is seen to be only about 1% of $\langle\overline{Q_1^\beta}\rangle$, with maximum value on the order of 5 W·m^{-2}.

The dynamic term of the β-model in Equation (4) is $\rho_a C_E \beta T_o' \Delta h$, and the thermodynamic term[1] is $\rho_a C_E \overline{U} \Delta h$. The ratio of these terms, which is a measure of the turbulent heat flux that is attributable to the mesoscale eddies, is then $\beta T_o'/\overline{U}$. Since $\overline{U}$ is close to 10 m·s^{-1} throughout the domain across all years, T_o' is generally less than 2 K, and the average β is 0.25, the ratio of the dynamic term to the thermodynamic term $\beta T_o'/\overline{U}$ is expected to be $<(0.25 \times 2)/10 = 5\%$. The time mean of this ratio is shown in Figure 7b for the winter of 2007; as expected, it generally does not exceed 5%. In order for the dynamic term to be 10% of the thermodynamic term in the β-model, T_o' would need to be at least 4 K. We return in Section 5 to a discussion of the magnitude of the high-pass-filtered SST anomalies in ERA5.

[1]We use this nomenclature to emphasize the difference between changes in winds ("dynamic") and changes in moisture and temperature fields ("thermodynamic"), but we acknowledge that both terms are shaped by dynamical adjustments of the marine boundary layer to mesoscale SST anomalies.

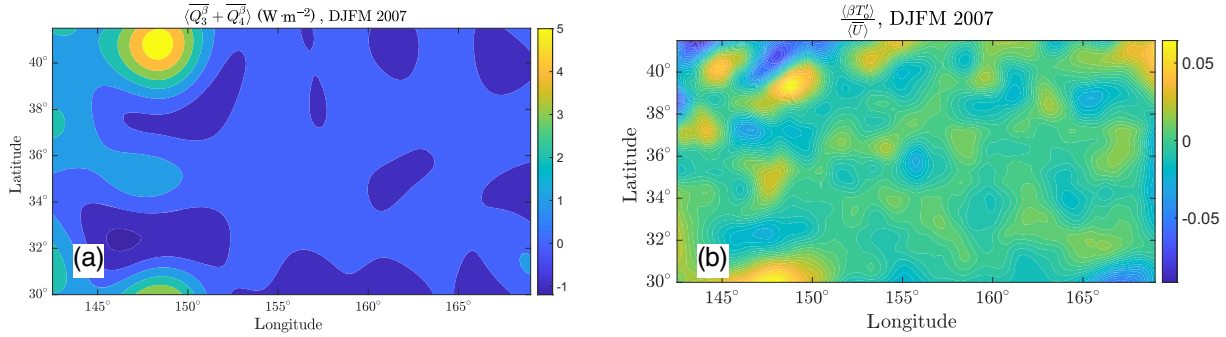

FIGURE 7 (a) The sum of the rectified effect terms $\langle \overline{Q_3^\beta} + \overline{Q_4^\beta} \rangle$ and (b) the ratio of the time mean of the dynamic term $\langle \beta T_o' \Delta h \rangle$ to the time mean of the thermodynamic term $\langle \overline{U} \Delta h \rangle$ of the β-model for the winter (DJFM) of 2007 [Colour figure can be viewed at wileyonlinelibrary.com]

4.2 | The $\alpha\beta$-model

The effect of mesoscale SST fluctuations on stability is now included by writing

$$C_E = C_E^{(ref)}(1 + \alpha T_o'), \tag{8}$$

where α is another coupling coefficient capturing the effect of T_o' on the exchange coefficient C_E. Continuing with Equation (4), we obtain

$$Q^{\alpha\beta} = \rho_a C_E^{(ref)}(1 + \alpha T_o')(\overline{U} + \beta T_o')\Delta h. \tag{9}$$

In this new model, the three optimized parameters are β (as in the first model), $C_E^{(ref)}$ (which is a reference or "background" value for the exchange coefficient), and the eddy coupling coefficient α (which when positive indicates an enhancement of the surface heat exchange over a warm mesoscale eddy).

This model also shows good agreement with the ERA5 data (see Figure S2). The mean and standard deviations of the three model parameters α, β, and C_E across all years considered are $\alpha = -3.3 \times 10^{-4} \pm 0.01\,K^{-1}$, $\beta = 0.29 \pm 0.09\,m{\cdot}s^{-1}{\cdot}K^{-1}$, and $C_E^{(ref)} = (1.4 \pm 0.01) \times 10^{-3}$. In this model it appears that the β term is sufficient to characterize the eddy-enhanced flux, as the optimized α coupling coefficient varies between positive and negative values in different years such that it effectively vanishes in the time mean across 2003–2018. As in the previous model, the long-time, large spatial-scale term dominates the other terms. The ratio of the dynamic terms to the thermodynamic terms in this model is $(\overline{U}\alpha T_o' + \beta T_o' + \alpha\beta(T_o')^2)/\overline{U}$. Using the average values of the model parameters, $\overline{U} = 10\,m{\cdot}s^{-1}$, and T_o' <2 K again, the expected upper bound for this ratio is approximately 5.8%. This bound is very similar to that from the β-model due to the small time-averaged value of α, and the plot of this ratio for the winter of 2007 is shown in Figure S4.

5 | DISCUSSION

The two models presented in Section 4 are successful at representing the air–sea turbulent heat flux from the reanalysis fields, and each isolates eddy contributions through different mechanisms using only one or two eddy coupling coefficients. The optimized values for all parameters and all the models, shown in Figure S1, are found to be relatively stable from winter to winter. Neither the values of the eddy coupling coefficients (Figure S1) nor the RMSEs (Figures 5 and S3) appear to be sensitive to the degree of stability of the Kuroshio's path over a winter. The RMSEs calculated between the model and the ERA5 fields using the optimal value of the coupling coefficients are less than 20 W·m^{-2} for all models and all years considered. The goal of the $\alpha\beta$-model was to understand the relative importance of the different eddy coupling coefficients α and β, and the results suggest that the β coefficient alone is able to capture the signal from the eddies. This roughly agrees with the findings reviewed by Small *et al.* (2008), in which the sea-surface drag enhancement of the surface wind stress was a smaller effect than the changes in atmospheric stability from the warm and cold eddies that drive near-surface winds.

A more difficult issue to address is that of the magnitude of the mesoscale SST signals T_o', which we have estimated using an FFT-based high-pass filter with a cutoff wavelength of 500 km. Figure 8 shows a histogram of the normalized frequency of the time mean high-pass-filtered SST $\langle T_o' \rangle$ from each winter overlaid with a normalized histogram of the six-hourly high-pass-filtered SST from all winters. The minimum and maximum values in the $\langle T_o' \rangle$ distribution are −3.6 K and 3.0 K, and in the synoptic distribution they are −7.9 K and 6.2 K. Although there are a few outliers, and the synoptic set has a slightly broader distribution, more than 98% of the points in the $\langle T_o' \rangle$ distribution and more than 97% of the points in the synoptic distribution are within ±2 K. As a result of these weak

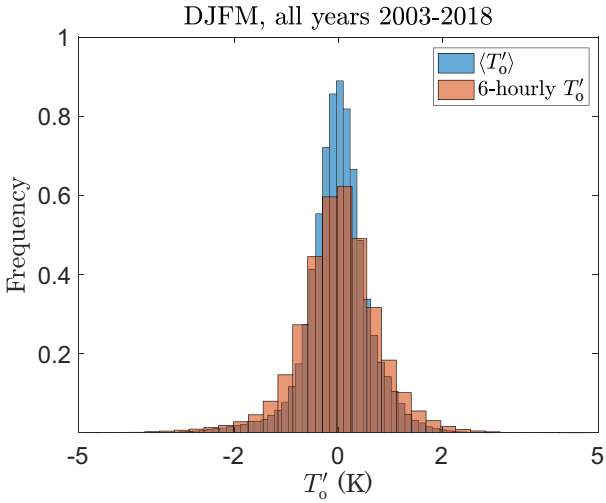

FIGURE 8 The blue histogram shows the normalized frequency of the time mean $\langle T'_o \rangle$ of each winter (DJFM), and the orange histogram shows the normalized frequency of the six-hourly T'_o for all winters [Colour figure can be viewed at wileyonlinelibrary.com]

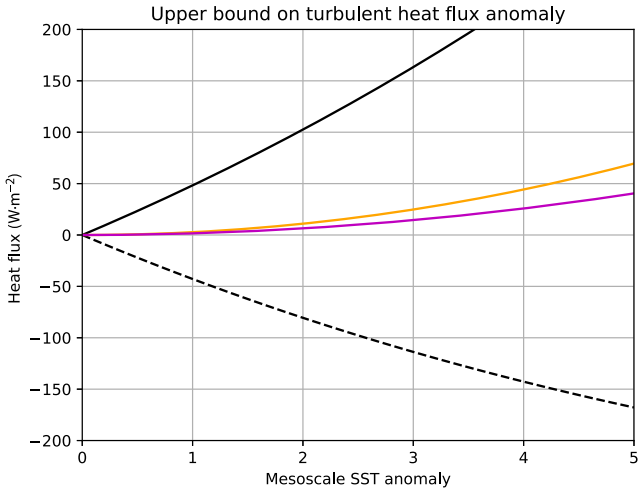

FIGURE 9 Upper bound on the turbulent heat flux in response to a positive (continuous black) and negative (dashed black) mesoscale sea-surface off temperature (SST) anomaly, as given by Equation (11) with a large-scale wind speed $\overline{U} = 10\,\mathrm{m{\cdot}s^{-1}}$ and unperturbed SST of 15° C (other parameters are $C_E = 1.4 \times 10^{-3}$ and $\beta = 0.25\,\mathrm{m{\cdot}s^{-1}{\cdot}^\circ\,C^{-1}}$). The residual, the sum of the continuous and dashed curve divided by two, is shown in orange. The case when β is set to zero is shown in magenta [Colour figure can be viewed at wileyonlinelibrary.com]

values of T'_o, the contribution of the rectified effect to the time series of the turbulent heat flux is difficult to see. Figure 4 demonstrates this difficulty; the resultant heat flux when β is set to zero (dashed green line) can be compared with the full calculation ($\beta = 0.25\,\mathrm{m{\cdot}s^{-1}{\cdot}^\circ\,C^{-1}}$ as discussed previously in Section 4.1 and displayed as the continuous green curve). Even though the time series was chosen to be in the region where the rectified effect is maximized (148.5° E, 41° N), the two simulated time series are barely distinguishable from one another.

The small values of T'_o appear to explain the smaller influence of the eddies from ERA5 compared with those found in other studies (Ma *et al.*, 2017; Foussard *et al.*, 2019). The SST anomalies in Ma *et al.* (2017) are approximately 3 K, whereas many of the anomalies in Foussard *et al.* (2019, fig. 3) are nearly 6 K, resulting in turbulent heat fluxes attributable to the mesoscale eddies on the order of $10\,\mathrm{W{\cdot}m^{-2}}$. Indeed, the asymmetry between anomalous cooling of a warm mesoscale SST feature and the anomalous warming of a cold one increases with the absolute value of the SST (equal to unperturbed + perturbation). This can be seen in the β-model by considering the limit case in which atmospheric dynamics efficiently remove any temperature and moisture anomalies arising in the marine boundary layer in response to a mesoscale SST fluctuation. Denoting the latter by $\delta T'_o$, the thermodynamic contrast Δh between air and water in Equation (4) then changes, in this limit, in direct proportion to the change in the oceanic state:

$$\delta(\Delta h) \approx \left(\frac{dh_o}{dT_o}\right) \delta T'_o. \tag{10}$$

In this expression, we have introduced $h_o = c_p T_o + l_v q^\star_o$, which is a monotonically increasing function of SST (both linearly through the $c_p T_o$ term and nonlinearly through the Clausius–Clapeyron relation included in $q^\star_o$). Because the adjustment of the marine boundary layer is ignored in Equation (10), and that the latter would tend to weaken the thermodynamic contrast between air and seawater ($\Delta h \to 0$), the resulting change in the magnitude $|\delta Q_\beta|$ of the turbulent heat flux is bounded by

$$|\delta Q_\beta| \le \rho_a C_E (\overline{U} + \beta \delta T'_o) \left(\frac{dh_o}{dT_o}\right) |\delta T'_o|. \tag{11}$$

The right-hand side of Equation (11) is plotted in Figure 9 for positive (continuous black) and negative (dashed black) $\delta T'_o$, and the residual (half the sum) is shown by the orange curve. For a value $\overline{U} = 10\ \mathrm{m \cdot s^{-1}}$ and an unperturbed SST of 15° C, the residual is found to be on the order of $3\,\mathrm{W{\cdot}m^{-2}}$ for $T'_o = 1^\circ$ C, $11\,\mathrm{W{\cdot}m^{-2}}$ for $T'_o = 2^\circ$ C, and $25\,\mathrm{W{\cdot}m^{-2}}$ for $T'_o = 3^\circ$ C. Note that the residual computed here is enhanced significantly beyond that predicted by Clausius–Clapeyron by the presence of the dynamical coupling β (see the case $\beta = 0$ plotted in magenta, which thus only includes the Clausius–Clapeyron nonlinearity). The values of a few watts per square meter found in our analysis (Figure 6) are thus consistent with the small range of SST anomaly displayed in Figure 8.

The key issue revealed by our analysis is thus the magnitude of the SST fluctuations brought about by either

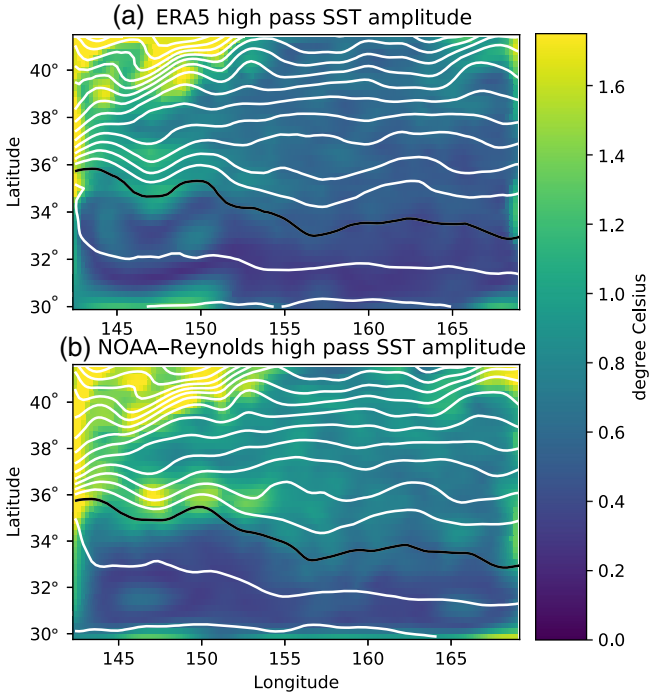

FIGURE 10 Amplitude of high-pass sea-surface temperature (SST) fields T_o' for (a) the ERA5 and (b) the NOAA–Reynolds SST fields. The amplitude is shown in color, and the mean SST field is shown by white contours, with a contour interval of 1° C (18° C isotherm in black for reference). The analysis was performed for DJFM winters from 2003 to 2018, and the amplitude was computed using the fast Fourier transform-based filter described in Section 2. Daily data were used for NOAA–Reynolds and six-hourly data were used for ERA5 [Colour figure can be viewed at wileyonlinelibrary.com]

traveling eddies or quasi-steady meanders of the Kuroshio and Oyashio currents. To test how sensitive figures like Figure 8 are to the particular SST datasets considered in this region, we have compared the variance of T_o' in the ERA5 data with another dataset of similar resolution, the so-called NOAA–Reynolds SST dataset (Reynolds *et al.*, 2007). The result, shown in Figure 10, suggests that the mesoscale SST anomalies are indeed weaker in ERA5, especially along the KE (they span the range 1.25–1.75° C in the NOAA–Reynolds product but only 1–1.25° C in ERA5), whereas the amplitudes in the northwestern corner of our domain, associated with the Oyashio SST front, are more comparable (1.75–2.25° C). The implication is that our estimate of the rectified contribution to the turbulent surface cooling might be underestimated along the KE and that this contributes to the lack of correlation seen in Section 3. Despite the higher variability seen in the NOAA–Reynolds SST product, Equation (11) and Figure 9 suggest that the residual heat flux is, however, unlikely to exceed 10 $W \cdot m^{-2}$ there (using the range of amplitude mentioned earlier; i.e., 1.25–1.75° C).

A couple of recent studies have indeed suggested that ERA5 may struggle to accurately estimate SST near western boundary currents. Yang *et al.* (2021) conducted a detailed comparison of eight SST products, including ERA5 and OSTIA (Donlon *et al.*, 2012), which is used within ERA5, for the years 2003–2018. Their results of the time-averaged difference of monthly SSTs between each product and the median of all the products showed that ERA5 generally agreed well with the ensemble median except for a few locations, including regions near western boundary currents. Near the KE in particular, they found that, on average, ERA5 underestimated the SST by a small fraction of a degree Celsius compared with the ensemble median. Though that study considered the total SST rather than the mean and anomaly separately, and compared ERA5 with other SST products rather than observations, the notable discrepancies in western boundary current regions that exhibit higher mesoscale eddy activity might indicate that ERA5 underestimates the magnitude of the SST fluctuations in this region. Luo and Minnett (2020) compared the SST from ERA5 with ship-based radiometric measurements and found that, though the two datasets generally agreed well, large air–sea temperature differences, such as those that are present near the Gulf Stream, tend to increase the error between ERA5 and observations. Though that study was focused on the Atlantic, the results show that near the Gulf Stream the discrepancy between the observations and ERA5 was as large as 1.5 K.

6 | SUMMARY AND CONCLUSIONS

The main results of our study can be summarized as follows:

- A two-parameter model for the surface turbulent heat flux (the "β-model") is able to simulate accurately its spatial structure and time variability over the KE region in winter.
- The model allows for separation of the impact of mesoscale structures present in the SST field, defined here as smaller than 500 km, on the larger scale averaged surface cooling, an effect that we have referred to as the "rectified effect."
- Using ERA5 data, the rectified effect was estimated to be on the order of a few watts per square meter for the wintertime mean, peaking in the region of the Oyashio front. This order of magnitude can be understood from the strength of the large-scale winds, the strength of the coupling coefficient β, the unperturbed value of the SST, and the amplitude of the mesoscale SST fluctuations—see Equation (11).

- Of these controlling factors, the latter is probably the most uncertain, and our estimate is likely biased low because of the weaker amplitude of mesoscale SST variability in ERA5 compared with other SST products. Nevertheless, it is unlikely that the rectified effect would increase beyond $10\,W{\cdot}m^{-2}$ even considering the larger amplitude of this (high-pass) variability in other SST products.
- The weak value of the rectified effect over the KE, in addition to atmospheric variability, can explain the lack of a robust relationship between the state of this current and the turbulent surface heat flux in the Northwest Pacific in wintertime.

Although the overall magnitude of the rectified effect might appear quite small (a few percent at most of the wintertime mean surface turbulence in this region), it has been shown in idealized models, regional climate models, and global models (Ma *et al.*, 2017; Foussard *et al.*, 2019; Zhang *et al.*, 2020) to be able to shift the North Pacific storm track with a magnitude, depending on the metric chosen, on the order of a few tens of percent—that is, a large sensitivity. This suggests that a better understanding of what controls the amplitude of the mesoscale SST variability, and the timescale on which it varies, is an important avenue of future research. For example, we note that the analysis carried out with the time mean T'_o for each winter yielded very similar results to that using the full SST field (not shown), suggesting a weaker effect of transient features, such as traveling or detached eddies, than of quasi-stationary meanders of the Oyashio and Kuroshio on the rectified effect in ERA5.

Finally, although our motivation came from an atmospheric perspective, the idealized models of air–sea interaction developed here might be useful to understand the role of mesoscale features present in the SST field and the surface turbulent heat fluxes on the general circulation of the ocean. Recent work has indeed shown a role for these interactions in the oceanic energy cycle and the mixed-layer heat budget that goes well beyond the small numbers highlighted in our study (Bishop *et al.*, 2020; Shan *et al.*, 2020).

AUTHOR CONTRIBUTIONS

Sydney Sroka: data curation, formal analysis, investigation, methodology, software, visualization. **Arnaud Czaja:** conceptualization; supervision; validation. **Soumi Chakravorty:** investigation; resources; validation.

ACKNOWLEDGEMENTS

This study has been conducted using E.U. Copernicus Marine Service Information. Hersbach *et al.* (2018) was downloaded from the Copernicus Climate Change Service Climate Data Store, and the NCEP–NCAR reanalysis was downloaded from the LDEO Climate Data Library. This work was supported by an MIT Office of Graduate Education Fellowship.

CONFLICT OF INTEREST

The authors declare no conflicts of interest.

ORCID

Sydney Sroka https://orcid.org/0000-0002-8225-7568

REFERENCES

Behringer, D., Regier, L. and Stommel, H. (1979) Thermal feedback on wind-stress as a contributing cause of the Gulf Stream. *Journal of Marine Research*, 37, 699–709.

Bishop, S.P., Small, R.J. and Bryan, F.O. (2020) The global sink of available potential energy by mesoscale air–sea interaction. *Journal of Advances in Modeling Earth Systems*, 12, e2020MS002118

Bishop, S.P., Small, R.J., Bryan, F.O. and Tomas, R.A. (2017) Scale dependence of midlatitude air–sea interaction. *Journal of Climate*, 30, 8207–8221.

Cayan, D.R. (1992) Latent and sensible heat flux anomalies over the northern oceans: Driving the sea surface temperature. *Journal of Physical Oceanography*, 22, 859–881.

Chelton, D.B., Schlax, M.G., Freilich, M.H. and Milliff, R.F. (2004) Satellite measurements reveal persistent small-scale features in ocean winds. *Science*, 303, 978–983. https://doi.org/10.1126/science.1091901

Chelton, D.B. and Xie, S.-P. (2010) Coupled ocean–atmosphere interaction at oceanic mesoscales. *Oceanography*, 23, 52–69.

Donlon, C.J., Martin, M., Stark, J., Roberts-Jones, J., Fiedler, E. and Wimmer, W. (2012) The Operational Sea Surface Temperature and Sea Ice Analysis (OSTIA) system. *Remote Sensing of Environment*, 116, 140–158. https://doi.org/10.1016/j.rse.2010.10.017

Drévillon, M., Regnier, C., Lellouche, J., Garric, G., Bricaud, C. and Hernandez, O. (2018). CMEMS-GLO-QUID-001-030, 1.2 edn. Available at: https://resources.marine.copernicus.eu/documents/QUID/CMEMS-GLO-QUID-001-030.pdf. [Accessed May 18, 2020].

Foussard, A., Lapeyre, G. and Plougonven, R. (2019) Storm track response to oceanic eddies in idealized atmospheric simulations. *Journal of Climate*, 32, 445–463.

Frankignoul, C. (1985) Sea surface temperature anomalies, planetary waves, and air–sea feedback in the middle latitudes. *Reviews of Geophysics*, 23, 357–390.

Global Monitoring and Forecasting Center (2018). GLORYS12V1—Global Ocean Physical Reanalysis product. Available at: https://resources.marine.copernicus.eu/?option=com_csw&view=details&product_id=GLOBAL_REANALYSIS_PHY_001_030. [Accessed May 18, 2020].

Hersbach, H., Bell, B., Berrisford, P., Biavati, G., Horányi, A., Muñoz Sabater, J., Nicolas, J., Peubey, C., Radu, R., Rozum, I., Schepers, D., Simmons, A., Soci, C., Dee, D. and Thépaut, J.-N. (2018). ERA5 hourly data on single levels from 1979 to present. Available at: https://cds.climate.copernicus.eu/cdsapp#!/dataset/reanalysis-era5-single-levels?tab=overview [Accessed April 20, 2020].

Hersbach, H., Bell, B., Berrisford, P., Hirahara, S., Horányi, A., Muñoz-Sabater, J., Nicolas, J., Peubey, C., Radu, R., Schepers, D., Simmons, A., Soci, C., Abdalla, S., Abellan, X., Balsamo, G., Bechtold, P., Biavati, G., Bidlot, J., Bonavita, M., De Chiara, G., Dahlgren, P., Dee, D., Diamantakis, M., Dragani, R., Flemming, J., Forbes, R., Fuente, M.S., Geer, A., Haimberger, L., Healy, S., Hogan, R.J., Hólm, E., Janisková, M., Keeley, S., Laloyaux, P., Lopez, P., Lupu, C., Radnoti, G., de Rosnay, P., Rozum, I., Vamborg, F., Villaume, S. and Thépaut, J.-N. (2020) The ERA5 global reanalysis. *Quarterly Journal of the Royal Meteorological Society*, 146, 1999–2049.

Hoskins, B.J. and Valdes, P.J. (1990) On the existence of storm-tracks. *Journal of the Atmospheric Sciences*, 47(15), 1854–1864.

Kalnay, E., Kanamitsu, M., Kistler, R., Collins, W., Deaven, D., Gandin, L., Iredell, M., Saha, S., White, G., Woollen, J., Zhu, Y., Chelliah, M., Ebisuzaki, W., Higgins, W., Janowiak, J., Mo, K.C., Ropelewski, C., Wang, J., Leetmaa, A., Reynolds, R., Jenne, R. and Joseph, D. (1996) The NCEP/NCAR 40-year reanalysis project. *Bulletin of the American Meteorological Society*, 77, 437–472.

Luo, B. and Minnett, P.J. (2020) Evaluation of the ERA5 sea surface skin temperature with remotely-sensed shipborne marine–atmospheric emitted radiance interferometer data. *Remote Sensing*, 12(11), 1873

Ma, J., Xu, H., Dong, C., Lin, P. and Liu, Y. (2015) Atmospheric responses to oceanic eddies in the Kuroshio Extension region. *Journal of Geophysical Research: Atmospheres*, 120, 6313–6330.

Ma, X., Chang, P., Saravanan, R., Montuoro, R., Hsieh, J.-S., Wu, D., Lin, X., Wu, L. and Jing, Z. (2015) Distant influence of Kuroshio eddies on North Pacific weather patterns?. *Scientific Reports*, 5, 17785. https://doi.org/10.1038/srep17785

Ma, X., Chang, P., Saravanan, R., Montuoro, R., Nakamura, H., Wu, D., Lin, X. and Wu, L. (2017) Importance of resolving Kuroshio front and eddy influence in simulating the North Pacific storm track. *Journal of Climate*, 30, 1861–1880.

Ma, X., Jing, Z., Chang, P., Liu, X., Montuoro, R., Small, R.J., Bryan, F.O., Greatbatch, R.J., Brandt, P., Wu, D., Lin, X. and Wu, L. (2016) Western boundary currents regulated by interaction between ocean eddies and the atmosphere. *Nature*, 535, 533–537.

Nakamura, H., Sampe, T., Tanimoto, Y. and Shimpo, A. (2004). Observed associations among storm tracks, jet streams and midlatitude oceanic fronts. In C. Wang, S.P. Xie, and J.A. Carton (Eds.), *Earth's Climate: The Ocean–Atmosphere Interaction*, Geophysical Monograph Series (Vol. 147 pp. 329–345). Washington, DC: American Geophysical Union.

O'Neill, L.W., Chelton, D.B. and Esbensen, S.K. (2010) The effects of SST-induced surface wind speed and direction gradients on midlatitude surface vorticity and divergence. *Journal of Climate*, 23, 255–281. https://doi.org/10.1029/147GM18

Putrasahan, D.A., Miller, A.J. and Seo, H. (2013) Isolating mesoscale coupled ocean–atmosphere interactions in the Kuroshio Extension region. *Dynamics of Atmospheres and Oceans*, 63, 60–78.

Qiu, B. and Chen, S. (2005) Variability of the Kuroshio extension jet, recirculation gyre, and mesoscale eddies on decadal time scales. *Journal of Physical Oceanography*, 35, 2090–2103.

Qiu, B. and Chen, S. (2006) Decadal variability in the formation of the North Pacific Subtropical Mode Water: Oceanic versus atmospheric control. *Journal of Physical Oceanography*, 36(7), 1365–1380. https://doi.org/10.1175/JPO2918.1

Qiu, B., Chen, S., Schneider, N., Oka, E. and Sugimoto, S. (2020) On the reset of the wind-forced decadal Kuroshio Extension variability in late 2017. *Journal of Climate*, 33(24), 10813–10828. https://doi.org/10.1175/JCLI-D-20-0237.1

Reynolds, R.W., Smith, T.M., Liu, C., Chelton, D.B., Casey, K.S. and Schlax, M.G. (2007) Daily high-resolution-blended analyses for sea surface temperature. *Journal of Climate*, 20(22), 5473–5496. https://doi.org/10.1175/2007JCLI1824.1

Scott, R.B. and Wang, F. (2005) Direct evidence of an oceanic inverse kinetic energy cascade from satellite altimetry. *Journal of Physical Oceanography*, 35, 1650–1666.

Shan, X., Jing, Z., Gan, B., Wu, L., Chang, P., Ma, X., Wang, S., Chen, Z. and Yang, H. (2020) Surface heat flux induced by mesoscale eddies cools the Kuroshio–Oyashio extension region. *Geophysical Research Letters*, 47(1), e2019GL086050. https://doi.org/10.1029/2019GL086050

Small, R., de Szoeke, S., Xie, S., O'Neill, L., Seo, H., Song, Q., Cornillon, P., Spall, M. and Minobe, S. (2008) Air–sea interaction over ocean fronts and eddies. *Dynamics of Atmospheres and Oceans*, 45(3–4), 274–319. https://doi.org/10.1016/j.dynatmoce.2008.01.001

Tulloch, R., Marshall, J., Hill, C. and Smith, K.S. (2011) Scales, growth rates, and spectral fluxes of baroclinic instability in the ocean. *Journal of Physical Oceanography*, 41, 1057–1076.

Villas Bôas, A., Sato, O., Chaigneau, A. and Castelão, G. (2015) The signature of mesoscale eddies on the air–sea turbulent heat fluxes in the South Atlantic Ocean. *Geophysical Research Letters*, 42, 1856–1862.

Yang, C., Leonelli, F.E., Marullo, S., Artale, V., Beggs, H., Nardelli, B.B., Chin, T.M., De Toma, V., Good, S., Huang, B., Merchant, C.J., Sakurai, T., Santoleri, R., Vazquez-Cuervo, J., Zhang, H.-M. and Pisano, A. (2021) Sea surface temperature intercomparison in the framework of the Copernicus Climate Change Service (C3S). *Journal of Climate*, 34(13), 5257–5283. https://doi.org/10.1175/JCLI-D-20-0793.1

Zhang, C., Liu, H., Xie, J., Lin, P., Li, C., Yang, Q. and Song, J. (2020) North Pacific storm track response to the mesoscale SST in a global high-resolution atmospheric model. *Climate Dynamics*, 55, 1597–1611.

SUPPORTING INFORMATION

Additional supporting information can be found online in the Supporting Information section at the end of this article.

How to cite this article: Sroka, S., Czaja, A. & Chakravorty, S. (2022) Assessing the importance of mesoscale sea-surface temperature variations for surface turbulent cooling of the Kuroshio Extension in wintertime. *Quarterly Journal of the Royal Meteorological Society*, 148(747), 2742–2754. Available from: https://doi.org/10.1002/qj.4333